

Histopathological Image Classification With Color Pattern Random Binary Hashing-Based PCANet and Matrix-Form Classifier

Jun Shi, Jinjie Wu, Yan Li, Qi Zhang, and Shihui Ying, *Member, IEEE*

Abstract—The computer-aided diagnosis for histopathological images has attracted considerable attention. Principal component analysis network (PCANet) is a novel deep learning algorithm for feature learning with the simple network architecture and parameters. In this study, a color pattern random binary hashing-based PCANet (C-RBH-PCANet) algorithm is proposed to learn an effective feature representation from color histopathological images. The color norm pattern and angular pattern are extracted from the principal component images of R, G, and B color channels after cascaded PCA networks. The random binary encoding is then performed on both color norm pattern images and angular pattern images to generate multiple binary images. Moreover, we rearrange the pooled local histogram features by spatial pyramid pooling to a matrix-form for reducing the dimension of feature and preserving spatial information. Therefore, a C-RBH-PCANet and matrix-form classifier-based feature learning and classification framework is proposed for diagnosis of color histopathological images. The experimental results on three color histopathological image datasets show that the proposed C-RBH-PCANet algorithm is superior to the original PCANet and other conventional unsupervised deep learning algorithms, while the best performance is achieved by the proposed feature learning and classification framework that combines C-RBH-PCANet and matrix-form classifier.

Index Terms—Color angular pattern, color histopathological image, color norm pattern, matrix-form classifier, PCANet, random binary hashing.

I. INTRODUCTION

HIGH-RESOLUTION histopathological image provides a reliable view of the underlying tissue, and diagnosis from

Manuscript received April 18, 2016; revised July 11, 2016; accepted August 20, 2016. Date of publication August 25, 2016; date of current version September 1, 2017. This work was supported in part by the National Natural Science Foundation of China (61471231, 61401267, 61471245, 11471208, U1201256), the Innovation Program of Shanghai Municipal Education Commission (13YZ016), and the Projects of Guangdong R/D Foundation and the Fundamental Science Projects of Shenzhen City (JCYJ20140418091413514, ZDSYS20140508141148477, JCYJ20160308095019383).

J. Shi, J. Wu, and Q. Zhang are with the Institute of Biomedical Engineering, School of Communication and Information Engineering, Shanghai University, Shanghai 200444 China (e-mail: junshi@staff.shu.edu.cn; Jinjie_Wu@shu.edu.cn; zhangqi@shu.edu.cn).

Y. Li is with the Shenzhen City Key Laboratory of Embedded System Design, Shenzhen Laboratory of IC Design for Internet of Things, College of Computer Science and Software Engineering, Shenzhen University Shenzhen, 518060 China (e-mail: liyan@szu.edu.cn).

S. Ying is with the Department of Mathematics, School of Science, Shanghai University, Shanghai, 200444 China (Corresponding author. e-mail: shyang@shu.edu.cn).

Digital Object Identifier 10.1109/JBHI.2016.2602823

histopathological image remains the “gold standard” for almost all types of cancer [1], [2]. There is a pressing need for the computer-aided diagnosis (CAD) or quantitative analysis of histopathological images now [1]–[4]. Diagnosing the presence of cancer (image classification) is one of the clinical important tasks for histopathological image-based CAD, which has attracted considerable attention in recent years.

Feature representation is a critical factor in the histopathological image-based CAD. Numerous feature extraction methods have been proposed to represent the local cell-level information (e.g., size and shape) or holistic architecture of tissue (e.g., topology and layout of all cells) from histopathological images [1], [4]. These commonly used features can be roughly divided into three categories: 1) the object-level features that characterize biological structure, including the size and shape, radiometric and densitometric, texture, and chromatin specific [1], [4], [5]; 2) the spatial-related features that quantify cellular arrangement or other structures and are usually derived from the graph-based algorithms, such as Delaunay, Voronoi, minimum spanning graph and connected graph [1], [4], [5], [6]; and 3) the multiscale-based features, e.g., multiresolution approach, pyramid and hierarchical feature representation algorithms [1], [4], [5], [6]. For the review of the histopathological image classification with hand-crafted features, we refer to [1], [4], [5], [6]. Despite the appreciable progress of various feature extraction methods for histopathological images, the hand-crafted features usually have poor transfer ability. It is still a challenging task to design effective feature descriptors due to the complicity and diversity of histopathological images.

In recent years, representation learning, which automatically learns useful information and discovers appropriate representation directly from data instead of hand-crafted features [7]–[9], has gained its good reputation for histopathological images. As a typical representation learning method, sparse representation and its variants have shown their effectiveness for histopathological images [10]–[14]. More recently, deep learning (DL) has also been applied to histopathological images. DL is almost the most successful representation learning method now. DL is suitable to learn feature representation for histopathological images, as it can directly learn effective image representation from pixel (or low) level features to discover high-level shape and edge interactions [7], [8]. In the last couple of years, various DL algorithms, such as convolutional neural networks, autoencoder, and its variants, have been applied to histopathological images

for classification and detection, and achieved the state-of-the-art performance [5], [15]–[20].

Despite the wide applications of various DL algorithms, they usually suffer from the problem of parameter tuning, which is not only time costing, but also in need of much expertise knowledge. The principal component analysis network (PCANet) is a novel framework for unsupervised DL, which consists of only three simple basic components: cascaded PCA as a deep network, binary hashing as a nonlinear layer, and block-wise histograms for feature pooling layer [21]. The network architecture of PCANet is very simple with few parameters. Moreover, PCANet indeed achieves competitive and even better performance for image classification compared with other state-of-the-art DL algorithms [21], [22]. Several improved PCANet algorithms are then proposed, such as DLANet [23], SRDANet [24], and SPCANet [25]. The successful application of PCANet for image representation makes it feasible to histopathological images.

The variants of PCANet mainly focus on applying more effective filters instead of PCA in the PCANet framework to improve representation performance. In fact, the way of binary hashing in PCANet also affects the representation performance, which has not been deeply investigated yet. In current PCANet and its variants, the binary hashing approach just simply encodes the quantized binary values according to the sequence of principal components (PC), that is to say, the first PC is assigned to the most significant bit, while the last PC is corresponding to the least significant bit [21]. It is worth noting that the current binary hashing operator is one of the n^2 binary codes for an n -bit vector, therefore, only limited information is obtained, which affects classification performance. Random theory-based methods, such as the random subspace and random projection algorithms, have been widely used in machine learning. Motivated by the success of the random methods, we propose to perform random binary hashing (RBH) in PCANet (named RBH-PCANet). RBH will not consider the sequence of PCs, but randomly encode these binary codes of PCs for several times, which then generate multiple random binary hashing codes. Consequently, more codes can provide more information for image representation.

On the other hand, hematoxylin and eosin (H&E) staining is commonly performed to reveal cellular components and enhance visibility of spatial structures of histological components in histopathology. Therefore, color information is helpful for pathologists, and color descriptors have been effectively used for histopathological images [1], [2]. Since PCANet algorithm is mainly applied to grayscale images [21], [23]–[25], the conversion of color image to grayscale should be conducted first. As a result, plenty of useful color information is discarded leading to reduced performance for color histopathological images. Although PCANet can be implemented on each individual color channel to generate multichannel features for concatenation, this way ignores the inherent correlation among different color channels of histopathological images [1]. Therefore, it is crucial to integrate color information into PCANet for learning representation of histopathological images.

Recently, Lee *et al.* have proposed a local color vector binary patterns (LCVBP) algorithm to effectively represent color face images [26]. In LCVBP, color information is integrated into local binary pattern (LBP) by two different patterns, namely the color norm pattern of a color vector and the color angular patterns between pairs of pixels of a color vector [26]. In order to fuse color information into PCANet, motivated by the effectiveness of LCVBP for color images, we also propose a color pattern-based PCANet (C-PCANet) algorithm.

Pattern classification is another important step in CAD. The conventional classifiers are generally resorted to the vector-form features. The local histogram features extracted from PCANet are usually concatenated to form a feature vector, which not only has a very high dimensionality resulting in the curse of dimensionality, but also destroy the spatial structure information or inherent correlation [27]. The spatial pyramid pooling (SPP) algorithm can be connected to the output layer of PCANet to improve the performance of PCANet by integrating spatial information [21], [28]. However, in SPP, the final feature vector is the concatenation of pooled features from different pooling layers. Therefore, the feature dimensionality is very high. Moreover, although the SPP algorithm can integrate the spatial information of image from local histogram features and generate more efficient image feature representation, there is still some loss of spatial structure information between multiple pooling layers in SPP by concatenating features from different layers.

Recently, some matrix-based classifiers have been proposed, which can more effectively classify matrix-form features that have captured more spatial information [27], [29]–[32]. Therefore, as one of the solutions for the aforementioned problem of SPP, the pooled local PCANet features after SPP can be arranged to a matrix-form to reduce feature dimensionality and partially maintain spatial information, and then fed to a matrix feature based classifier. Here, a newly proposed low-rank bilinear classifier (LRBC) is used in this work due to its excellent classification performance for matrix-form features [30], [31].

In this study, we propose a new feature learning and classification framework to solve a specific clinical problem, namely, the color histopathological image-based CAD for cancer. The proposed framework consists of a color pattern random binary hashing-based PCANet (named C-RBH-PCANet hereafter with C indicating color encoding) algorithm and a matrix-based classifier. The main contributions are threefold: 1) the C-PCANet algorithm is proposed by building the color norm pattern and angular pattern so as to effectively extract color information from color histopathological images, and then well fuse and represent color histopathological images; 2) The C-RBH-PCANet algorithm is proposed to further improve the representative performance, which performs the random binary hashing on color pattern images to generate multiple binary codes with more representative information; and 3) Instead of concatenating features in the traditional SPP, the pooled local histogram features by SPP are arranged to form the matrix-form features to maintain the spatial structure information among multiple layers, which are then fed to the matrix-based classifier to achieve improved classification performance for histopathological images.

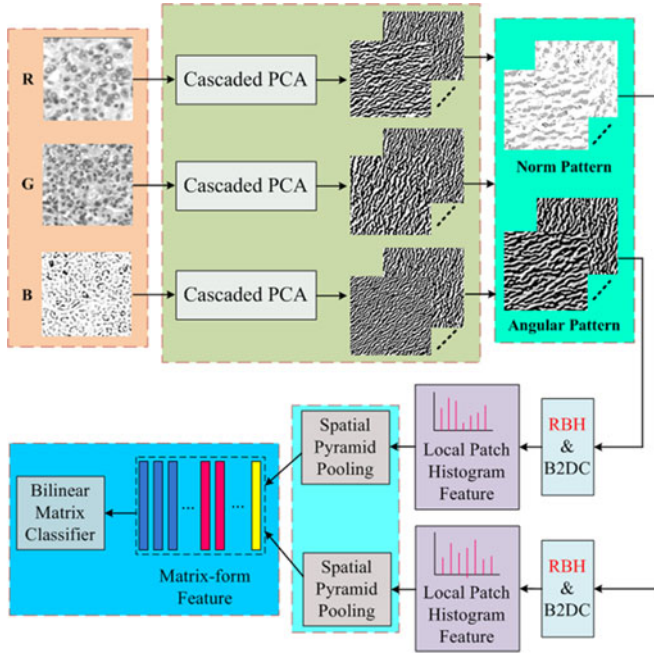


Fig. 1. Flowchart of the proposed C-RBH-PCANet and matrix-form classifier-based framework for classification of color histopathological images.

II. METHOD

Fig. 1 shows the proposed feature learning and classification framework, including C-RBH-PCANet, SPP and matrix-form classifier. C-RBH-PCANet algorithm is applied to color histopathological images to generate local histogram features, which consists of four basic components: cascaded PCA, color patterns, random binary hashing, and block-wise histograms. In details, the cascaded PCA is conducted on the R, G, and B channels of color histopathological images, respectively, to generate a sequence of PC images. The color norm pattern and angular pattern images are then extracted by fusing a group of PC images belong to R, G, and B channels, respectively. The RBH is performed on both color norm pattern images and angular pattern images to generate multiple binary images, from which local histogram features are extracted and then hierarchically pooled by SPP. Finally, the pooled features from SPP are arranged to the matrix-form features, which are fed to a bilinear matrix-form classifier for classification. Here, the LRBC algorithm is selected as the matrix-form classifier because of its effectiveness.

A. Color Pattern Random Encoding-Based PCANet

1) **Cascaded PCA Network:** For a color histopathological image, the cascaded PCA is first performed on individual R, G, B channels, respectively. As shown in Fig. 2, the basic flowchart of cascaded PCA network is introduced as follows [21].

In the first stage of the PCA network, a training set of image patches is taken from all the training images to train a PCA model. Then, we can achieve m leading components for each patch around each pixel in all the training images. Notably, each

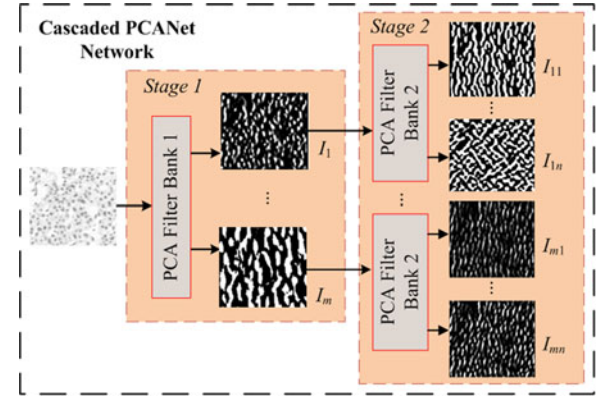


Fig. 2. Flowchart of cascaded PCA network.

leading component will be set as a new pixel value with the same location corresponding to the original pixel. Therefore, a training image will generate m PC images after the first stage of PCA network.

Almost repeating the same process in the first stage, the second stage PCA network can be easily built with m PC images as the root images. For each root PC image, n new PC image are generated. After filtering by the two-stage cascaded PCA networks, there are totally $m \times n$ real-valued output images generated from an initial input image.

It is worth noting that more PCA stages can be built by simply repeating the aforesaid process.

In this study, a color histopathological image will be separated into R, G, and B channels, and then a two-layer cascaded PCA network will perform on individual R, G, and B channels. Therefore, $3 \times m \times n$ real-valued images in total are generated for color feature extraction.

2) **Extraction of Color Patterns:** As can be seen from Fig. 3, in order to extract the color norm pattern and angular pattern, let $c = [v_{(x,y)}^R, v_{(x,y)}^G, v_{(x,y)}^B]$ denote a color vector, where $v_{(x,y)}^R$, $v_{(x,y)}^G$, and $v_{(x,y)}^B$ are the pixel values of R, G, and B images at the location (x, y) . The color norm value is then defined by [26]

$$r = \|c\| = \sqrt{v_{(x,y)}^R{}^2 + v_{(x,y)}^G{}^2 + v_{(x,y)}^B{}^2}. \quad (1)$$

Thus, three color channel images can be easily fused into a norm image by computing the r -value pixel by pixel.

The ratio of pixel values between a pair of color channels is first calculated by [26]

$$\varphi^{(p,q)} = \frac{v_p}{v_q + \gamma} \quad (2)$$

where p and q represent the arbitrary two channels among R, G or B images, while v_p and v_q are the corresponding pixel values in p and q channel images, respectively, and γ is a small-valued constant to avoid a zero value of v_q . Since the ratio of pixel values provides the directional information of a color vector, the discriminative color angular pattern is then extracted by defining the color angle between p and q color channels [26]

$$\theta^{(i,j)} = \tan^{-1} \left(\varphi^{(p,q)} \right). \quad (3)$$

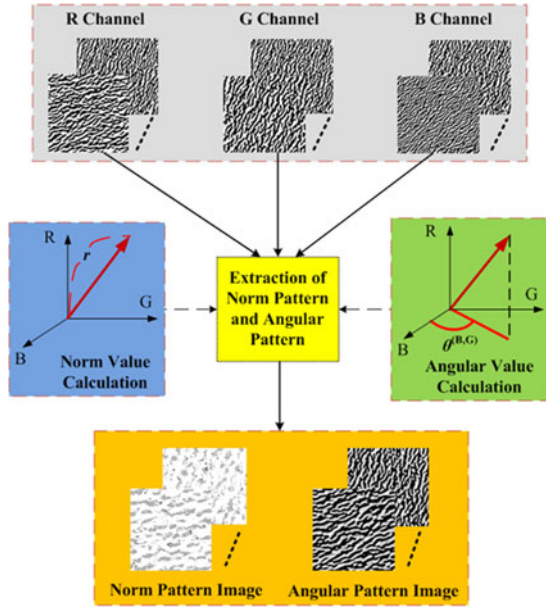


Fig. 3. Illustration of extracting color norm pattern and color angular pattern from R, G, and B channel images.

Define I_{ij}^R , I_{ij}^G and I_{ij}^B as the output PC images in R, G, and B channels, respectively, where i is the index of i th PC image in the first state PCA network ($i = 1, \dots, m$), and j is the index of j th PC image in the second stage ($j = 1, \dots, n$) corresponding to the i th root PC image. After extracting color norm pattern and angular pattern from $m \times n$ group of R, G, and B channel PC images, $2 \times m \times n$ images are produced. The RBH and extraction of local histogram features will then be conducted on these images, respectively.

3) Random Binary Hashing on Color Pattern Images and Block-Wise Histograms: In the original PCANet, a simple binary quantization (hashing) operator is performed on the $m \times n$ output images by a Heaviside step (like) function, whose value is one for positive entries and zero otherwise [21]. The binary pixel values at the same location are then regarded as an n -bit vector according to the sequence of PCs.

In our study, the simple binary hashing operator is improved by performing RBH on the color pattern images so as to generate richer features with color information, which is named C-RBH-PCANet.

A binary quantization operator is performed on both the color norm pattern images and angular pattern images. It is noteworthy that the mean value of all pixels in all $m \times n$ color norm pattern images is selected as the threshold of binary quantization rather than zero in original PCANet algorithm, because there is no negative value in color norm pattern images. For each group of n binary norm pattern images corresponding to the same root PC image in the first stage PCA network, we randomly encode the n binary pixel values at the same location (x, y) from n images without considering the sequence of PCs. This RBH operation repeats k times, which then generates k n -bit vectors for the same location (x, y) . As a consequence, the k vectors provide more useful information to represent images. The same

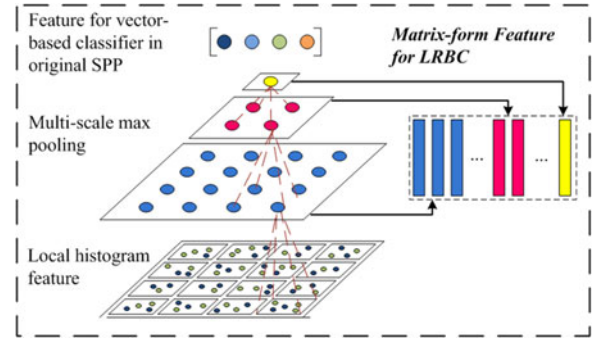


Fig. 4. Illustration of arranging pooled local features in different layers of SPP to a matrix-form feature.

operation is conducted on the color angular pattern images. After implementing RBH pixel by pixel, a total of $2 \times k \times m$ binary norm pattern images and angular pattern images are generated.

The binary to decimal conversion (B2DC) is then performed on these binary norm pattern images and angular pattern images after RBH, namely, each n -bit binary vector is then converted back into an integer value. Therefore, a new single integer-valued image can be generated [21].

Finally, each of the final $2 \times k \times m$ images is then partitioned into B blocks, and histograms of the decimal values are then computed in each block as local features.

It is worth noting that the way of binary encoding and local feature extraction in our study is totally different from that in the LCVBP algorithm. In LCVBP, the LBP operator is directly performed on both color norm pattern and angular pattern images by comparing the center pixel with its neighbors for binary encoding [26]. While in C-RBH-PCANet, the binary hashing is conducted by encoding the corresponding PC values at each pixel on both color norm pattern and angular pattern images. Moreover, the local histogram features are not directly extracted from either color norm pattern or angular pattern images, but from the B2DC-based images that are fused by binary hashing.

B. Spatial Pyramid Pooling

An input image generates totally $2 \times k \times m$ images by C-RBH-PCANet. For the local histogram features, SPP algorithm is then used for each image to effectively integrate spatial information in image by hierarchical pooling. For details of the SPP algorithm, readers can refer to [28].

As shown in Fig. 4, the pooled local features in different layers of SPP are arranged to a matrix-form. It is worth noting that for $2 \times m$ PC color pattern images belonging to the same encoding sequence of a RBH, their local histogram features in the same position are concatenated to form a vector with a dimensionality of $(256 \times 2) \times m$, where 256 is the feature dimensionality of local histogram. As shown in Fig. 4, these concatenated local features are then processed by SPP to build a matrix-form feature with a size of $(512 \times m) \times N_s$, where N_s is the total number of spatial bins in the multilayer pyramid. For example, the first, second, and third layers of the pyramid have 16, 4, and 1 bins in Fig. 4, respectively, and thus $N_s = 21$. Finally, k feature matrices in total are generated from k

RBH encoding sequences, each with a size of $(512 \times m) \times N_s$, and they are connected to form a large matrix with a size of $(512 \times m) \times (N_s \times k)$.

C. Low-Rank Bilinear Classifier

The matrix features arranged after SPP are then fed to a matrix-form classifier for classification, namely LRBC, which is introduced as follows [30], [31].

Let X be a $w \times h$ feature matrix ($X \in R^{w \times h}$). The multirank bilinear classifier is given by

$$\hat{y} = \text{tr}(M_w^T X M_h) + b = \text{tr}(M^T X) + b \quad (4)$$

where $\text{tr}(\cdot)$ is the trace of a matrix, b is the bias, and $M = M_w M_h^T \in R^{w \times h}$ is the classifier matrix ($M_w \in R^{w \times r}$, $M_h \in R^{h \times r}$ where $r \leq \min[w, h]$).

In the maximum-margin framework, the margin of bilinear classifier by matrix trace norm is measured to minimize the matrix rank, resulting in the following optimization problem

$$\min_{M, b} \|M\|_\epsilon + C \sum_{i=1}^n \max[0, 1 - y_i \{\text{tr}(M^T X_i) + b\}] \quad (5)$$

where $\|M\|_\epsilon$ indicates the trace norm of M for n sample pairs $\{X_i, y_i\}$.

The smoothing regularization is then applied to (5), which is expressed by the quadratic form derived from Laplacian of the weight with the formulation

$$\begin{aligned} & \min_{M_w, M_h, b} \frac{1}{2} \text{tr}(M_h M_h^T + M_w M_w^T) \\ & + \frac{1}{2} C_h \text{tr}(M_h^T L_h M_h) + \frac{1}{2} C_w \text{tr}(M_w^T L_w M_w) \\ & + C \sum_i \max[0, 1 - y_i \{\text{tr}(M_w^T X_i M_h) + b\}] \quad (6) \end{aligned}$$

where L_w, L_h are the matrices to measure the smoothness, and C_w, C_h are regularization parameters. Equation (6) is then reformulated to a tractable convex problem and the global optimum can be produced efficiently. For more detailed optimization solution and other information about LRBC, please refer to [30] and [31].

III. EXPERIMENT AND RESULTS

A. Experimental Design

To evaluate the proposed feature learning and classification framework based on C-RBH-PCANet and matrix-based classifier, three histopathological image datasets, namely the Massachusetts General Hospital (MGH) breast dataset [33], ADL kidney image dataset [34] and hepatocellular carcinoma (HCC) image dataset [12], are used in this study. MGH breast dataset was approved by the Partners Human Research Committee (Partners IRB) [33]. In this study, 34 images of ductal carcinoma *in situ* (DCIS) and 32 images of usual ductal hyperplasia (UDH) from MGH are included, and each has a size of 800×1800 . ADL dataset is kindly published by the Animal Diagnostics Lab (ADL), Pennsylvania State University [34]. We randomly

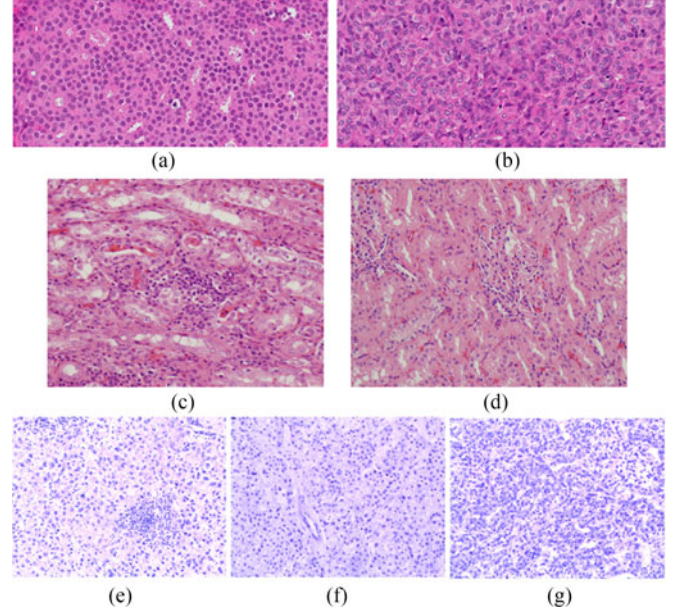


Fig. 5. Example images of three color histopathological image datasets. (a) and (b) are the DCIS image and UDH image in MGH dataset, respectively; (c) and (d) are the inflammatory image and health image in ADL-Kidney dataset, respectively; (e)–(g) are the well-differentiated liver image, moderately differentiated liver image, and poorly differentiated liver image in HCC dataset, respectively.

TABLE I
PARAMETERS OF SAE AND DBN USED FOR MGH DATASET

	SAE	DBN
Hidden node	180	100
Layer	3	2 RBMs
Batch size	500	200
Epoch	1000	2000

selected 100 kidney histopathological images (50 inflammatory images and 50 healthy images) with a size of $1,360 \times 1,024$ pixel. The HCC dataset was acquired with Olympus BX51 from Medical College, Nantong University, Nantong, China, which includes 66 HCC images (21 well-differentiated images, 23 moderately differentiated images, and 22 poorly differentiated images) with a size of $1,024 \times 768$ [12]. Fig. 5 shows the example images of different datasets.

Experiments are conducted on grayscale histopathological images and color histopathological images, respectively, to evaluate different algorithms. For grayscale histopathological images converted from color images, RBH-PCANet is compared with the original PCANet, sparse coding (SC) [35], and two commonly used unsupervised DL algorithms, namely stacked autoencoder (SAE) and deep belief network (DBN) [36], [37]. For color images, C-RBH-PCANet is compared with C-PCANet and the concatenated three-channel features of PCANet on R, G, and B images (named RGB-PCANet), in which PCANet is performed on R, G, and B channels, respectively, and the learned three channel features are then concatenated to form a color feature vector. Tables I–III show the parameters of SAE and DBN

TABLE II

PARAMETERS OF SAE AND DBN USED FOR ADL-KIDNEY DATASET

	SAE	DBN
Hidden node	100	100
Layer	3	2 RBMs
Batch size	400	200
Epoch	1000	600

TABLE III

PARAMETERS OF SAE AND DBN USED FOR HCC DATASET

	SAE	DBN
Hidden node	110	130
Layer	3	2 RBMs
Batch size	500	100
Epoch	600	800

TABLE IV

CLASSIFICATION RESULTS OF DIFFERENT FEATURE LEARNING ALGORITHMS WITH SVM CLASSIFIER ON GRAYSCALE IMAGES OF MGH DATASET (UNIT: %)

	ACC	SEN	SPE
SC	63.03 \pm 3.65	67.06 \pm 2.46	58.39 \pm 6.08
DBN	70.91 \pm 1.66	74.37 \pm 5.07	67.28 \pm 2.71
SAE	71.21 \pm 2.14	82.35 \pm 0.00	59.38 \pm 4.42
PCANet	70.61 \pm 2.30	78.82 \pm 1.31	61.88 \pm 3.42
RBH-PCANet	72.42 \pm 0.68	81.76 \pm 1.32	62.50 \pm 2.21

for different datasets, which are fine-tuned to achieve the best performance. All the PCANet-based algorithms have two layer networks, and each patch generates eight PCs in each layer. All the aforementioned features are fed to the linear support vector machine (SVM) for fair comparison [38]. Moreover, to evaluate the effectiveness of matrix-form features arranged after SPP, LRBC algorithm is compared with SVM on the learned features by C-RBH-PCANet.

For all SC, SAE, DBN, PCANet, and its variants algorithms, 10 000 patches are randomly sampled from the training set images of each dataset to learn individual feature representation model. The patch sizes are 11×11 , 17×17 , and 17×17 pixels for the images in MGH dataset, ADL-Kidney dataset, and HCC dataset, respectively. RBH method is performed four times for all RBH embedded PCANet for all datasets, which generates four binary codes. In the SPP procedure, the local patches are densely sampled without overlapping in each image.

The leave-one-out strategy is used to evaluate the classification performance for each dataset. We repeat the aforesaid experiments five times to calculate the averaged results. The classification accuracy, sensitivity, and specificity are selected as evaluation indices. A paired-sample *t*-test is used to statistically evaluate the performances of the proposed algorithm. The results are declared statistically significant if the *p*-value is less than 0.05. Moreover, the receiver operating characteristic (ROC) curve and the value of the area under ROC curve (AUC) are also used to evaluate the algorithms for the binary-class task.

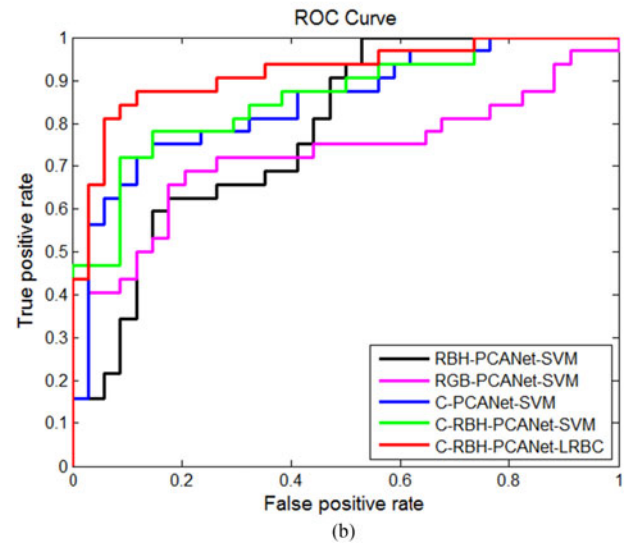
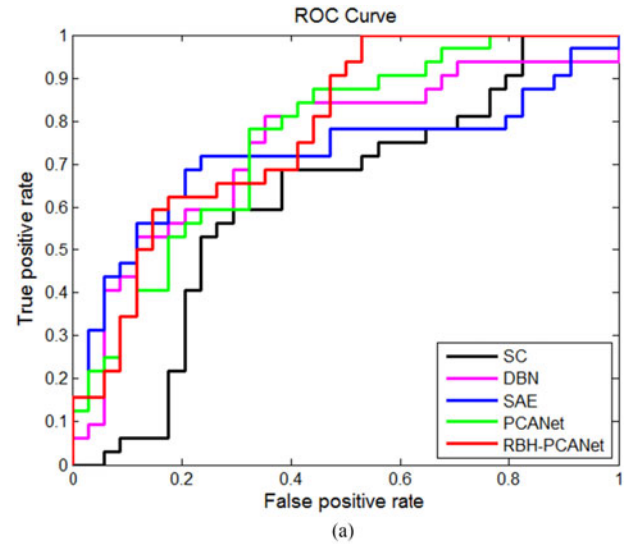


Fig. 6. ROC curves of different algorithms on MGH dataset. (a) ROC curves of different algorithms for grayscale histopathological images and (b) ROC curves of different algorithms for color histopathological images.

B. Results on MGH Breast Image Dataset

Table IV shows the results of different feature learning algorithms on grayscale images of MGH dataset with SVM classifier. It can be found that RBH-PCANet achieves the best classification accuracy of $72.42 \pm 0.68\%$ and gets the second place on sensitivity of $81.76 \pm 1.32\%$ and specificity of $62.50 \pm 2.21\%$. SAE and DBN get the best sensitivity and specificity, respectively. Compared with the original PCANet, RBH-PCANet improves 1.81% of classification accuracy, 2.94% of sensitivity, and 0.62% of specificity, which indicates the effectiveness of RBH in PCANet. Fig. 6(a) shows the ROC curves of different algorithms, and the corresponding AUC values are shown in Table VII. RBH-PCANet outperforms all the compared algorithms for grayscale images with an AUC value of 0.779.

Table V gives the results of different PRCANet-based algorithms on color images of MGH dataset with SVM classifier

TABLE VII

AUC VALUES OF DIFFERENT ALGORITHMS ON MGH DATASET

Grayscale Images	AUC	Color Images	AUC
SC	0.584	RBH-PCANet-SVM	0.779
DBN	0.689	RGB-PCANet-SVM	0.685
SAE	0.682	C-PCANet-SVM	0.812
PCANet	0.766	C-RBH-PCANet-SVM	0.824
RBH-PCANet	0.779	C-RBH-PCANet-LRBC	0.884

TABLE V

CLASSIFICATION RESULTS OF DIFFERENT FEATURE LEARNING ALGORITHMS ON COLOR IMAGES OF MGH DATASET (UNIT: %)

	ACC	SEN	SPE
RBH-PCANet-SVM	72.42 \pm 0.68	81.76 \pm 1.32	62.50 \pm 2.21
RGB-PCANet-SVM	66.97 \pm 6.78	77.06 \pm 1.31	56.25 \pm 2.21
C-PCANet-SVM	76.97 \pm 1.98	76.47 \pm 4.65	77.50 \pm 1.40
C-RBH-PCANet-SVM	78.48 \pm 1.66	81.76 \pm 3.83	75.00 \pm 2.21
C-RBH-PCANet-LRBC	81.51 \pm 2.91	82.35 \pm 4.65	80.63 \pm 2.61

TABLE VI

RESULTS OF PAIRED-SAMPLE T-TEST FOR THE EVALUATION INDEXES OF C-RBH-PCANET-LRBC VERSUS OTHER ALGORITHMS WITH SVM CLASSIFIER

	ACC	SEN	SPE
SC	<0.05	<0.05	<0.05
DBN	<0.05	<0.05	<0.05
SAE	<0.05	1.000	<0.05
PCANet	<0.05	0.141	<0.05
RBH-PCANet	<0.05	0.793	<0.05
RGB-PCANet	<0.05	<0.05	<0.05
C-PCANet	<0.05	0.081	<0.05
C-RBH-PCANet	0.078	0.832	<0.05

or LBRC. For easy comparison, the results of RBH-PCANet with SVM on grayscale images are also shown in this table. For SVM classifier, RGB-PCANet even performs worse than RBH-PCANet on grayscale images. However, C-PCANet still improves 4.55% and 15.00% on classification accuracy and specificity, respectively, compared with RBH-PCANet. Moreover, C-RBH-PCANet with SVM further outperforms C-RBH-PCANet with the improvements of 1.51% on classification accuracy and 5.29% on sensitivity. Notably, C-RBH-PCANet with LRBC achieves the best performance over all other compared algorithms, whose classification accuracy, sensitivity, and specificity are $81.51 \pm 2.91\%$, $82.35 \pm 4.65\%$, and $80.63 \pm 2.61\%$, respectively. For the same C-RBH-PCANet features, LRBC makes improvements of 3.03%, 0.59%, and 5.63% in terms of classification accuracy, sensitivity, and specificity, respectively, compared with SVM. As shown in Table VI, C-RBH-PCANet-LRBC achieves significant improvement over all the compared algorithms on classification accuracy ($p < 0.05$) only except C-RBH-PCANet, and it also significantly superior to all other algorithms on specificity ($p < 0.05$). C-RBH-PCANet-LRBC also gets the best AUC

TABLE VIII

CLASSIFICATION RESULTS OF DIFFERENT FEATURE LEARNING ALGORITHMS WITH SVM CLASSIFIER ON GRAYSCALE IMAGES OF ADL-KIDNEY DATASET (UNIT: %)

	ACC	SEN	SPE
SC	79.80 \pm 2.59	78.00 \pm 1.41	81.60 \pm 3.84
DBN	77.60 \pm 1.34	72.40 \pm 2.19	82.80 \pm 1.09
SAE	82.40 \pm 1.52	86.40 \pm 0.89	78.40 \pm 2.19
PCANet	82.40 \pm 1.95	84.80 \pm 2.28	80.00 \pm 2.45
RBH-PCANet	83.20 \pm 1.64	85.60 \pm 2.19	80.80 \pm 1.79

value (0.884) in Table VII with the corresponding ROC curve in Fig. 6(b).

C. Results on ADL-Kidney Image Dataset

Table VIII shows the classification results of different feature learning algorithms with SVM classifier for grayscale images of ADL-Kidney dataset. RBH-PCANet achieves the best classification accuracy ($83.20 \pm 1.64\%$) and a second in sensitivity ($85.60 \pm 2.19\%$). SAE and DBN get the best sensitivity and specificity. All the three indices of RBH-PCANet are again superior to the original PCANet algorithm. RBH-PCANet also gets the best AUC value (0.856) in Table XI for grayscale images, and its ROC curve is shown in Fig. 7(a).

Table IX gives the classification results of different feature learning algorithms on ADL-Kidney images. It is seen that both RGB-PCANet and C-PCANet are superior to RBH-PCANet, suggesting that colors truly provide helpful information for feature representation of histopathological images. C-PCANet outperforms RGB-PCANet with improvements of 1.80% and 5.20% on classification accuracy and sensitivity, which shows that the color norm pattern and angular pattern for binary hashing in PCANet can more effectively fuse color information from different color channels. When combining color patterns and RBH together, C-RBH-PCANet with SVM achieves the second overall performance, which further makes improvements of 2.80% and 6.40% on classification accuracy and specificity, compared with C-PCANet. It is worth noting that C-RBH-PCANet with LRBC obtains overall best classification accuracy of $90.06 \pm 2.19\%$, sensitivity of $92.40 \pm 2.96\%$ and specificity of $88.80 \pm 2.68\%$, and improves 1.06%, 1.20%, and 2.00% compared with C-RBH-PCANet with SVM. It is also found in Table X that C-RBH-PCANet-LRBC significantly outperforms all compared algorithms except C-RBH-PCANet on both classification accuracy and specificity ($p < 0.05$), and it has significant improvement over all the algorithms except C-PCANet and C-RBH-PCANet on sensitivity. As shown in Fig. 7(b) and Table XI, C-RBH-PCANet-LRBC outperforms all compared algorithms on the AUC value (0.958).

D. Results on HCC Image Dataset

As shown in Tables XII and XIII, the results on HCC image dataset have a similar tendency to these of ADL-Kidney and MGH datasets. As can be seen from Table XII that for SVM classifier, RBH-PCANet achieves the best performance on grayscale

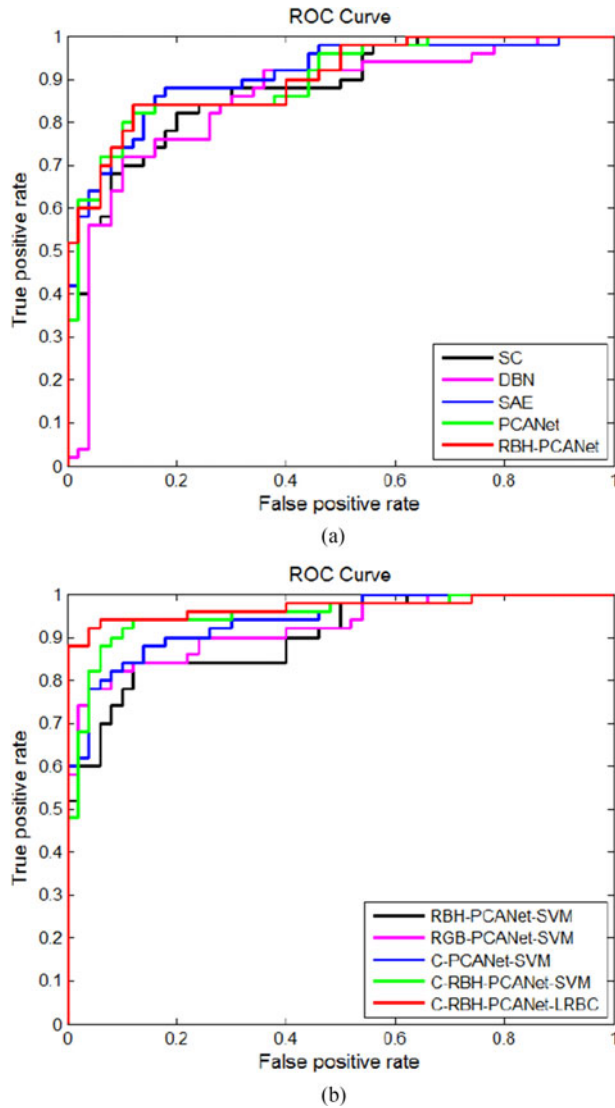


Fig. 7. ROC curves of different algorithms on ADL-Kidney dataset. (a) ROC curves of different algorithms for grayscale histopathological images and (b) ROC curves of different algorithms for color histopathological images.

image among all algorithms, whose classification accuracy, sensitivity, and specificity are $93.03 \pm 0.83\%$, $92.89 \pm 0.82\%$, and $96.50 \pm 0.42\%$, respectively, improved by at least 3.94%, 4.10%, and 2.01%. PCANet achieves the second-best performance, and it improves 3.64%, 3.68%, and 1.76% for accuracy, sensitivity, and specificity, respectively, as compared to SC, DBN, and SAE. RBH-PCANet also achieves significant improvement over all the compared algorithms in Table VIII on classification accuracy, sensitivity, and specificity ($p < 0.05$).

Table XIII shows the results of different algorithms on the color image of HCC dataset except the first row. Although both C-PCANet and C-RBH-PCANet outperform RGB-PCANet, the overall results of C-PCANet and C-RBH-PCANet on color images and PCANet on grayscale images are close when using SVM classifier. C-RBH-PCANet with LRBC achieves the best results in all performance measurements, whose classification accuracy, sensitivity, and specificity are $94.85 \pm 0.83\%$,

TABLE IX

CLASSIFICATION RESULTS OF DIFFERENT FEATURE LEARNING ALGORITHMS ON COLOR IMAGES OF ADL-KIDNEY DATASET (UNIT: %)

	ACC	SEN	SPE
RBH-PCANet-SVM	83.20 ± 1.64	85.60 ± 2.19	80.80 ± 1.79
RGB-PCANet-SVM	84.40 ± 1.14	86.80 ± 1.10	82.00 ± 1.41
C-PCANet-SVM	86.20 ± 1.30	92.00 ± 2.00	80.40 ± 2.19
C-RBH-PCANet-SVM	89.00 ± 1.87	91.20 ± 2.28	86.80 ± 2.68
C-RBH-PCANet-LRBC	90.06 ± 2.19	92.40 ± 2.96	88.80 ± 2.68

TABLE X

RESULTS OF PAIRED-SAMPLE T-TEST FOR THE EVALUATION INDEXES OF C-RBH-PCANet-LRBC VERSUS OTHER ALGORITHMS WITH SVM CLASSIFIER

	ACC	SEN	SPE
SC	<0.05	<0.05	<0.05
DBN	<0.05	<0.05	<0.05
SAE	<0.05	<0.05	<0.05
PCANet	<0.05	<0.05	<0.05
RBH-PCANet	<0.05	<0.05	<0.05
RGB-PCANet	<0.05	<0.05	<0.05
C-PCANet	<0.05	0.810	<0.05
C-RBH-PCANet	0.250	0.494	0.273

TABLE XI

AUC VALUES ON ADL-KIDNEY DATASET

Grayscale Images	AUC	Color Images	AUC
SC	0.840	RBH-PCANet-SVM	0.856
DBN	0.806	RGB-PCANet-SVM	0.887
SAE	0.832	C-PCANet-SVM	0.921
PCANet	0.848	C-RBH-PCANet-SVM	0.916
RBH-PCANet	0.856	C-RBH-PCANet-LRBC	0.958

TABLE XII

CLASSIFICATION RESULTS OF DIFFERENT FEATURE LEARNING ALGORITHMS WITH SVM CLASSIFIER ON GRAYSCALE IMAGES OF HCC DATASET (UNIT: %)

	ACC	SEN	SPE
SC	85.45 ± 2.30	85.11 ± 2.21	92.73 ± 1.14
DBN	82.12 ± 2.71	82.22 ± 2.75	91.12 ± 1.38
SAE	85.15 ± 2.71	84.96 ± 2.78	92.57 ± 1.36
PCANet	89.09 ± 0.68	88.79 ± 0.71	94.49 ± 0.34
RBH-PCANet	93.03 ± 0.83	92.89 ± 0.82	96.50 ± 0.42

TABLE XIII

CLASSIFICATION RESULTS OF DIFFERENT FEATURE LEARNING ALGORITHMS ON COLOR IMAGES OF HCC DATASET (UNIT: %)

	ACC	SEN	SPE
RBH-PCANet-SVM	93.03 ± 0.83	92.89 ± 0.82	96.50 ± 0.42
RGB-PCANet-SVM	85.45 ± 1.36	85.15 ± 1.56	92.66 ± 0.73
C-PCANet-SVM	93.03 ± 0.83	92.86 ± 0.86	96.51 ± 0.42
C-RBH-PCANet-SVM	93.33 ± 0.83	93.16 ± 0.84	96.66 ± 0.41
C-RBH-PCANet-LRBC	94.85 ± 0.83	94.70 ± 0.86	97.36 ± 0.42

TABLE XIV

RESULTS OF PAIRED-SAMPLE T-TEST FOR EVALUATION INDEXES OF C-RBH-PCANET-LRBC VERSUS OTHER ALGORITHMS WITH SVM CLASSIFIER

	ACC	SEN	SPE
SC	<0.05	<0.05	<0.05
DBN	<0.05	<0.05	<0.05
SAE	<0.05	<0.05	<0.05
PCANet	<0.05	<0.05	<0.05
RBH-PCANet	<0.05	<0.05	<0.05
RGB-PCANet	<0.05	<0.05	<0.05
C-PCANet	<0.05	<0.05	<0.05
C-RBH-PCANet	0.067	<0.05	<0.05

$94.70 \pm 0.86\%$, and $97.36 \pm 0.42\%$, respectively, at least improved by 1.52%, 1.54%, and 0.70%. Again, as shown in Table XIV, C-RBH-PCANet-LRBC is significantly superior to all the compared algorithms except RBH-PCANet and C-RBH-PCANet on classification accuracy ($p < 0.05$), and it has significant improvement over all other algorithms on both sensitivity and specificity ($p < 0.05$).

IV. DISCUSSION

PCANet is a newly proposed DL algorithm, which has the advantage of simple network architecture with good performance for feature learning. In this study, we first evaluate the feasibility of PCANet for histopathological images, and the results on three datasets show that PCANet achieves competitive results compared with SC, SAE, and DBN.

The improved PCANet algorithms only focus on how to use more effective filters instead of PCA and ignore the importance of binary encoding methods in PCANet. In the current PCANet algorithm and its variants, the binary hashing simply encodes the binary values based on the order of PC. However, this method cannot ensure that it is the best encoding way, and it only provides very limited information. To address this issue, we propose the RBH method that randomly encodes the binary codes without considering the order of PC. With the increment of binary codes by RBH, more information is captured for image representation. In this study, although RBH is only performed three times, the results already show that RBH-PCANet can improve the representative performance for histopathological images compared with the original PCANet. It suggests that the binary encoding method in deed affects the performance of PCANet. Notably, more times of RBH can implement to generate more random binary codes, which can further improve PCANet's representation performance of. However, the feature dimensionality will also increase, which may result in the curse of dimensionality. Therefore, we only perform RBH three times.

The color information is very important for the decision of histopathological images. Although PCANet can be implemented on individual R, G, and B channels to learn three feature vectors, the concatenated features ignore the correlation among different color channels, and some weak features may also reduce the representative performance. To overcome these problems, we propose the C-PCANet algorithm by extracting

color norm pattern images and color angular pattern images for binary quantization and local feature extraction. The color norm pattern can effectively fuse different color channels to generate a complementary effect, while the color angular pattern aims to effectively encode the pattern of the multiple interband angles based on the spatial interactions among the R, G, and B channels. Since the angle value at a pixel location between a pair of color channels does not change even with the illumination alterations, color angular pattern has the robust illumination invariance for histopathological images. Moreover, both color patterns discover the intracorrelation among different color channels. Therefore, C-PCANet can effectively represent color information, which has been proved on three color histopathological image datasets.

We then combine RBH and color pattern methods and propose the C-RBH-PCANet for color histopathological images. With more information by RBH and color information from color norm pattern and angular pattern, C-RBH-PCANet is superior to all other compared feature learning algorithms for classification of color histopathological images. It is worth noting that the final local histogram features are not directly extracted from the color norm pattern images or angular pattern images, but extracted from a synthetical image, which is generated through the following procedures:

- 1) the color norm pattern images and color angular pattern images are extracted from the corresponding PC images of R, G, and B channels in the second stage PCA network;
- 2) both color norm pattern images and color angular pattern images are then quantized to generate binary images;
- 3) RBH is conducted by encoding the binary pixels of same location from the binary images generated in step 2, and then B2DC is performed to build final synthetically.

Therefore, the local feature extraction in C-RBH-PCANet is highly different from that in LCVBP.

In the original PCANet, m images are synthesized for local histogram feature extraction, where m is the number of PCs in the first stage of PCA network. While in C-RBH-PCANet, a total of $2 \times k \times m$ images are generated because of applying RBH, color norm pattern, and angular pattern. Consequently, the features fed to classifier have very high feature dimensionality resulting in the curse of dimensionality. Moreover, although SPP can effectively integrate spatial information from local histogram features, it still somewhat loses the intracorrelation among different pooling layers when simply concatenating the pooled features from different layers. Therefore, we propose rearranging the vector-form feature to the matrix-form feature so as to reduce feature dimensionality and preserve the spatial information among different pooling layers. Thus, the matrix feature-based classifier is used for matrix-form features. It can be found in Tables V, VII, and VIII that the C-RBH-PCANet and LRBC-based algorithm achieves the best performance on all three datasets, which indicates the effectiveness of our proposed C-RBH-PCANet and matrix-form classifier-based feature learning and classification framework for color histopathological images. Of course, other matrix-form classifiers, such as bilinear matrix classifier and support matrix machine [30]–[32], can be used instead of LRBC algorithms.

In future work, more binary coding methods for PC values in PCANet will be investigated to provide more effective and compact feature representation. For example, since too many PC images are generated by our C-RBH-PCANet from color histopathological image, resulting in the problem of a very high feature dimensionality with a small sample size, more effective hashing algorithms can be used to encode the PC values of all the PC images to simultaneously generate more compact binary codes and fuse features of different PC images [39], [40]. Moreover, to balance the computational complexity and effectiveness of feature representation, we should study how many times RBH should be performed. In addition, multiple kernel learning (MKL) methods have shown its effectiveness for classification of heterogeneous features. Since the synthesized images with different RBH codes on both color norm pattern images and angular pattern image have different attributions for image representation, they can be regarded as different feature views; therefore, the MKL-based LRBC may be used for superior classification of histopathological images. It is also worth noting that most of the histopathological images are stained by H&E protocol in clinical practice, and it is easy to separate the haematoxylin and eosin component images with color deconvolution. Therefore, we will also study the fusion of H and E images with other PCANet-based frameworks, such as MKL. Of course, other color spaces will also be investigated for histopathological images.

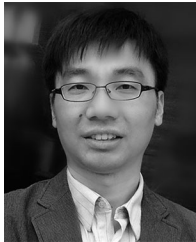
V. CONCLUSION

In this study, we propose an encoding improved PCANet algorithm, namely C-RBH-PCANet, to effectively integrate color pattern extraction and random binary hashing methods for learning feature representation from color histopathological images. C-RBH-PCANet is superior to the original PCANet. Moreover, we rearrange the histogram features generated by SPP to form a matrix, which is fed to the bilinear matrix-form feature-based LRBC classifier to further improve the classification performance. The proposed C-RBH-PCANet and matrix-form classifier based feature learning and classification framework achieves promising performance for diagnosis of color histopathological images on three datasets, suggesting its potential for the histopathology-based CAD system.

REFERENCE

- [1] M. N. Gurcan *et al.*, "Histopathological image analysis: A review," *IEEE Rev. Biomed. Eng.*, vol. 2, pp. 147–171, Oct. 2009.
- [2] H. Irshad, A. Veillard, L. Roux, and D. Racocceanu, "Methods for nuclei detection, segmentation and classification in digital histopathology: A review—current status and future potential," *IEEE Rev. Biomed. Eng.*, vol. 7, pp. 97–114, Dec. 2014.
- [3] M. Veta, J. P. W. Pluim, P. J. van Diest, and M. A. Viergever, "Breast cancer histopathology image analysis: A review," *IEEE Trans. Biomed. Eng.*, vol. 61, no. 5, pp. 1400–1411, May 2014.
- [4] C. M. Lopez, S. Agaian, A. V. Hoyos, and I. Thompson, "Computer-aided prostate cancer diagnosis from digitized histopathology: A review on texture-based systems," *IEEE Rev. Biomed. Eng.*, vol. 8, pp. 98–113, 2015.
- [5] J. Arevalo, A. C. Roa, V. Arias, E. Romero, and F. A. González, "An unsupervised feature learning framework for basal cell carcinoma image analysis," *Artif. Intell. Med.*, vol. 64, no. 2, pp. 131–145, 2015.
- [6] L. He, R. Long, S. Antani, and G. Thoma, "Histology image analysis for carcinoma detection and grading," *Comput. Methods Programs Biomed.*, vol. 107, no. 3, pp. 538–556, 2012.
- [7] Y. Bengio, A. Courville, and P. Vincent, "Representation learning: A review and new perspectives," *IEEE Trans. Pattern Anal. Mach. Intell.*, vol. 35, no. 8, pp. 1798–1828, Aug. 2013.
- [8] Y. LeCun, Y. Bengio, and G. E. Hinton, "Deep learning," *Nature*, vol. 521, pp. 436–444, 2015.
- [9] J. Wright *et al.*, "Sparse representation for computer vision and pattern recognition," *Proc. IEEE*, vol. 98, no. 6, pp. 1031–1044, Jun. 2010.
- [10] H. Chang, N. Nayak, P. T. Spellman, and B. Parvin, "Characterization of tissue histopathology via predictive sparse decomposition and spatial pyramid matching," in *Proc. 16th Int. Conf. Med. Image Comput. Comput. Assisted Intervention*, 2013, pp. 91–98.
- [11] U. Srinivas, H. S. Mousavi, V. Monga, A. Hattal, and B. Jayarao, "Simultaneous sparsity model for histopathological image representation and classification," *IEEE Trans. Med. Imag.*, vol. 33, no. 5, pp. 1163–1179, May 2014.
- [12] J. Shi, Y. Li, J. Zhu, H. J. Sun, and Y. Cai, "Joint sparse coding based spatial pyramid matching for classification of color medical image," *Comput. Med. Imag. Graph.*, vol. 41, pp. 61–66, 2015.
- [13] K. Sirinukunwattana, A. M. Khan, and N. M. Rajpoot, "Cell words: Modelling the visual appearance of cells in histopathology images," *Comput. Med. Imag. Graph.*, vol. 42, pp. 16–24, 2015.
- [14] H. Chang *et al.*, "Stacked predictive sparse decomposition for classification of histology sections," *Int. J. Comput. Vis.*, vol. 113, pp. 3–18, 2015.
- [15] D. C. Ciresan, A. Giusti, L. M. Gambardella, and J. Schmidhuber, "Mitosis detection in breast cancer histology images with deep neural networks," in *Proc. 16th Int. Conf. Med. Image Comput. Comput. Assisted Intervention*, 2013, pp. 411–418.
- [16] A. A. C. Roa, J. E. A. Ovalle, A. Madabhushi, and F. A. G. Osorio, "A deep learning architecture for image representation, visual interpretability and automated basal-cell carcinoma cancer detection," in *Proc. 16th Int. Conf. Med. Image Comput. Comput. Assisted Intervention*, 2013, pp. 403–410.
- [17] Y. P. Xie, F. Y. Xing, X. F. Kong, H. Su, and L. Yang, "Beyond classification: structured regression for robust cell detection using convolutional neural network," in *Proc. 18th Int. Conf. Med. Image Comput. Comput. Assisted Intervention*, 2015, pp. 358–365.
- [18] Y. Xu *et al.*, "Deep convolutional activation features for large scale Brain Tumor histopathology image classification and segmentation," in *Proc. IEEE Int. Conf. Acoust., Speech Signal Process.*, 2015, pp. 947–951.
- [19] J. Xu *et al.*, "Stacked sparse autoencoder (SSAE) for nuclei detection on breast cancer histopathology images," *IEEE Trans. Med. Imag.*, vol. 35, no. 1, pp. 119–130, Jan. 2016.
- [20] X. F. Zhang, H. Dou, T. Ju, J. Xu, and S. T. Zhang, "Fusing heterogeneous features from stacked sparse autoencoder for histopathological image analysis," *IEEE J. Biomed. Health Inform.*, vol. 75, no. 99, pp. 1–1, 2015.
- [21] T. H. Chan *et al.*, "PCANet: A simple deep learning baseline for image classification," *IEEE Trans. Image Process.*, vol. 24, no. 12, pp. 5017–5032, Dec. 2015.
- [22] S. K. Wang, L. Chen, Z. X. Zhou, X. Sun, and J. Y. Dong, "Human fall detection in surveillance video based on PCANet," *Multimedia Tools Appl.*, vol. 75, no. 19, pp. 1–11, 2015.
- [23] Z. Y. Feng, L. W. Jin, D. P. Tao, and S. P. Huang, "DLANet: A manifold-learning-based discriminative feature learning network for scene classification," *Neurocomputing*, vol. 157, pp. 11–21, Jun. 2015.
- [24] L. Tian, C. X. Fan, Y. Ming, and J. K. Shi, "SRDANet: an efficient deep learning algorithm for face analysis," in *Proc. 8th Int. Conf. Intell. Robot. Appl.*, 2015, pp. 499–510.
- [25] L. Tian, C. X. Fan, Y. Ming, and Y. Jin, "Stacked PCA network (SPCANet): an effective deep learning for face recognition," in *Proc. IEEE Int. Conf. Digital Signal Process.*, 2015, pp. 1039–1043.
- [26] S. H. Lee, J. Y. Choi, Y. M. Ro, and K. N. Plataniotis, "Local color vector binary patterns from multichannel face images for face recognition," *IEEE Trans. Image Process.*, vol. 21, no. 4, pp. 2347–2353, Apr. 2012.
- [27] C. P. Hou, F. P. Nie, C. S. Zhang, D. Y. Yi, and Y. Wu, "Multiple rank multilinear SVM for matrix data classification," *Pattern Recognit.*, vol. 47, pp. 454–469, 2014.
- [28] S. Lazebnik, C. Schmid, and J. Ponce, "Beyond bags of features: Spatial pyramid matching for recognizing natural scene categories," in *Proc. IEEE Conf. Comput. Vision Pattern Recog.*, 2006, pp. 2169–2178.
- [29] Z. Wang, S. Chen, J. Liu, and D. Zhang, "Pattern representation in feature extraction and classifier design: Matrix versus vector," *IEEE Trans. Neural Netw.*, vol. 19, no. 5, pp. 758–769, May 2008.

- [30] T. Kobayashi and N. Otsu, "Efficient optimization for low-rank integrated bilinear classifiers," in *Proc. Eur. Conf. Comput. Vision*, 2012, pp. 474–487.
- [31] T. Kobayashi, "Low-rank bilinear classification: efficient convex optimization and extensions," *Int. J. Comput. Vis.*, vol. 110, pp. 308–327, 2014.
- [32] L. Luo, Y. B. Xie, Z. H. Zhang, and W. J. Li, "Support matrix machines," in *Proc. 32nd Int. Conf. Mach. Learning*, 2015, pp. 938–947.
- [33] F. Dong *et al.*, "Computational pathology to discriminate benign from malignant intraductal proliferations of the breast," *PLOS One*, vol. 9, p. e114885, 2014.
- [34] U. Srinivas, H. S. Mousavi, C. Jeon, V. Monga, A. Hattel, and B. Jayarao, "SHIRC: A simultaneous sparsity model for histopathological image representation and classification," in *Proc. IEEE Int. Symp. Biomed. Imag.*, 2013, pp. 1106–1109.
- [35] J. C. Yang, K. Yu, Y. H. Gong, and T. Huang, "Linear spatial pyramid matching using sparse coding for image classification," in *Proc. IEEE Conf. Comput. Vision Pattern Recog.*, 2009, pp. 1794–1801.
- [36] Y. Bengio, P. Lamblin, D. Popovici, and H. Larochelle, "Greedy layerwise training of deep networks," in *Prof. Adv. Neural Inf. Process. Syst.*, 2006, pp. 153–160.
- [37] G. E. Hinton, S. Osindero, and Y. Teh, "A fast learning algorithm for deep belief nets," *Neural Comput.*, vol. 18, no. 7, pp. 1527–1554, 2006.
- [38] V. N. Vapnik, *Statistical Learning Theory*. New York, NY, USA: Wiley, 1998.
- [39] X. Zhang, W. Liu, M. Dundar, S. Badve, and S. Zhang, "Towards large-scale histopathological image analysis: Hashing-based image retrieval," *IEEE Trans. Med. Imag.*, vol. 34, no. 2, pp. 496–506, Feb. 2015.
- [40] M. Jiang, S. Zhang, J. Huang, L. Yang, and D. N. Metaxas, "Joint kernel-based supervised hashing for scalable histopathological image analysis," in *Proc. 18th Int. Conf. Med. Image Comput. Comput. Assisted Intervention*, 2015, pp. 366–373.



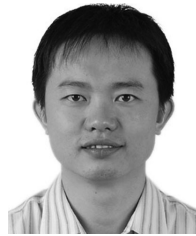
Jun Shi received the B.S. and Ph.D. degrees from the Department of Electronic Engineering and Information Science, University of Science and Technology of China, Hefei, China, in 2000 and 2005, respectively.

In 2005, he joined the Institute of Biomedical Engineering, School of Communication and Information Engineering, Shanghai University, Shanghai, China, where he has been a Professor since 2015. He was a Visiting Scholar in the Biomedical Research Imaging Center, University of North Carolina at Chapel Hill, Chapel Hill, NC, USA, from 2011 to 2012. His current research interests include medical image and signal processing, and pattern recognition in biomedical engineering.



Jinjie Wu received the B.S. degree from the School of Electrical and Information Engineering, Jiangsu University, Jiangsu, China, in 2013. He is currently working toward the M.Sc. degree in the School of Communication and Information Engineering, Shanghai University, Shanghai, China.

His research interests include the machine learning for medical images.



Yan Li received the B.Sc. degree from the University of Science and Technology of China, Hefei, China, in 2001, the M.Sc. degree from the Institut National des Sciences Appliquées de Toulouse, Toulouse, France, in 2003, and the Ph.D. degree from the University of Paris 11, Orsay, France, in 2007.

He is currently an Associate Professor in the College of Computer Science and Software Engineering, Shenzhen University, Shenzhen, China. His researches interests include VLSI

systems and data processing with machine learning.



Qi Zhang received the B.S. degree in electronic engineering in 2005 and the Ph.D. degree in biomedical engineering in 2010, both from Fudan University, Shanghai, China. From 2008 to 2009, he was a visiting Ph.D. Student at the Department of Biomedical Engineering, Duke University, Durham, NC, USA.

He joined the Institute of Biomedical Engineering, School of Communication and Information Engineering, Shanghai University, Shanghai, China in 2010. He is currently an Associate

Professor. His research interests include medical signal processing, biomedical modeling and computer aided diagnosis.



Shihui Ying (M'11) received the B.Eng. degree in mechanical engineering and the Ph.D. degree in applied mathematics from Xi'an Jiaotong University, Xi'an, China, in July 2001 and April 2008, respectively.

He is currently an Associate Professor in the Department of Mathematics, School of Science, Shanghai University, Shanghai, China. He was a Postdoctor in Biomedical Research Imaging Center, University of North Carolina at Chapel Hill, Chapel Hill, NC, USA, from 2012 to 2013.

His research interests cover mathematical theory and methods for medical imaging and image analysis.